

Notice

This is a non-peer reviewed preprint submitted to EarthArXiv. This manuscript has been submitted to Earth and Planetary Science Letters on Oct. 4 2019 with reference number EPSL-D-19-01365. Subsequent newer version may differ in text and content.

Details

Title: Crack to pulse transition and magnitude statistics during earthquake cycles on a self-similar rough fault

Author: Elías Rafn Heimisson

Contact: eheimiss@caltech.edu

Crack to pulse transition and magnitude statistics during earthquake cycles on a self-similar rough fault

Elías Rafn Heimisson^{a,*}

^a*Seismological Laboratory, California Institute of Technology, Pasadena, California, USA*

Abstract

Faults in nature demonstrate fluctuations from planarity at most length scales that are relevant for earthquake dynamics. These fluctuations may influence all stages of the seismic cycle; earthquake nucleation, propagation, arrest, and inter-seismic behavior. Here I show quasi-dynamic plane-strain simulations of earthquake cycles on a self-similar 10 km long rough fault with amplitude-to-wavelength ratio $\alpha = 0.01$. The minimum roughness wavelength, λ_{min} , and nucleation length scales are well resolved and much smaller than the fault length. Stress dissipation and fault loading is implemented using a variation of the backslip approach, which allows for efficient simulations of multiple cycles without stresses becoming unrealistically large. I explore varying λ_{min} for the same stochastically generated realization of a rough fractal fault. Decreasing λ_{min} causes the minimum and maximum earthquake sizes to decrease. Thus the fault seismicity is characterized by smaller and more numerous earthquakes, on the other hand, increasing the λ_{min} results in fewer and larger events. However, in all cases, the inferred b-value is constant and the same as for a reference no-roughness simulation ($\alpha = 0$). Further, the characteristics of individual ruptures are also altered and here I highlight a new mechanism for generating pulse-like ruptures. Seismic events are initially crack-like, but at a critical length scale, they continue to propagate as pulses, locking in an approximately fixed amount of slip. I investigate this transition using simple arguments and derive a characteristic pulse length and slip distance based on roughness drag. I hypothesize that the ratio λ_{min}/α^2 could be roughly estimated from kinematic rupture models. Furthermore, I suggest that the ergodicity of planar and rough fault simulations may be different.

Keywords: Rough faults, Rate-and-state friction, Earthquake cycle simulations,
Earthquake statistics, Earthquake ruptures, Pulses
2010 MSC: 00-01, 99-00

1. Introduction

Most modeling studies of earthquakes and the seismic cycle idealize faults as planar surfaces. However, a large body of work has shown that faults and rock surfaces are not planar [e.g. 1, 2, 3, 4, 5]. It has been established that fluctuations from planarity in faults are statistically fractal and self-affine (see Section 1.1 for details). It has become increasingly important to understand how and when planar models accurately capture key characteristics of individual ruptures as well as fault behavior during the entire seismic cycles.

Recently, several studies have simulated earthquakes on fractal faults. In most cases a single rupture is simulated, where the stress distribution and initial conditions are assumed before artificially nucleating the rupture [6, 7, 8, 9]. These studies have included many of the relevant physics such as off-fault plasticity and full elastodynamic effects. However, they are too computationally expensive to simulate multiple earthquake cycles which would include inter-seismic and post-seismic slip, as well as natural nucleation. This means that the assumed initial stress distribution may strongly influence the length and propagation characteristics of the simulated ruptures. A more complete approach would ideally allow stresses to evolve naturally over multiple cycles.

Other models have been developed that simulate the whole seismic cycle [10, 11, 12]. However, these methods lack a mechanism for stress dissipation, such as off-fault plasticity, and are purely elastic. This means that only a few cycles can be simulated before stresses build-up due to geometric incompatibility and reach unrealistic values. These studies cannot investigate behavior over multiple cycles. Recently, Allam et al., (2019) [13] used the RSQsim cycle simulator to simulate seismicity on a self-affine fault over multiple cycles. They used

*Corresponding author:

Email address: ehemiss@caltech.edu (Elías Rafn Heimisson)

23 a backslip to dissipate stresses and thus achieve an efficient way to simulate long term fault
 24 behavior. However, Allam et al. (2019) used oversized dislocations and did not resolve the
 25 relevant length-scales that arise from elasticity and the assumed friction law. Such models
 26 generally produce complex behavior that becomes simpler with grid refinement[14]. Since we
 27 expect fault roughness to produce complexity, it may be hard to untangle the contribution
 28 of the oversized dislocations versus the fault roughness.

29 Here I show results from a 2D plane-strain boundary element model with frictional
 30 properties governed by rate-and-state friction where state evolution evolves according to the
 31 aging law [15, 16]. The simulations are quasi-dynamic and implement a variation of the
 32 backslip approach to dissipate stresses. Thus unlike previous work, I report results from
 33 multiple cycles without unrealistic stress build-up, but at the same time, discretization is
 34 chosen such that all relevant lengths and time-scales are fully resolved. While many previous
 35 studies have focused on the amplitude-to-wavelength ratio of the roughness [e.g. 17, 9], I
 36 focus on systematically varying the minimum roughness wavelength of the fault. The range
 37 of λ_{min} explored is from 1/3 to 10 times the nucleation length for a planar fault.

38 1.1. Background

39 In this study, I investigate a strictly self-similar and statistically fractal fault. Self-
 40 similarity, in this case, implies the root-mean-square (RMS) fluctuations from planarity
 41 h_{RMS} are linearly proportional to the fault segment length L [3], in other words

$$h_{RMS} = \alpha L, \quad (1)$$

42 where α is the amplitude-to-wavelength ratio. Faults that obey such self-similarity have a
 43 power spectral density (PSD) [3]:

$$P_h(k) = (2\pi)^3 \alpha^2 |k|^{-3}, \quad (2)$$

44 where $k = 2\pi/\lambda$ is the wavenumber (λ is the wavelength). Fault roughness is often charac-
 45 terized in terms of the Hurst exponent H , where $h_{RMS} = \alpha L^H$, with $H = 1$ implying strict
 46 self-similarity. Fang and Dunham (2013) [7] showed that for a sufficiently long wavelength

47 slip on a self-similar fault, the average resistance to sliding due to geometric complexity is
 48 given by the roughness drag:

$$\tau_{drag} = 8\pi^3 \alpha^2 \frac{\mu}{1 - \nu} \frac{\delta}{\lambda_{min}}, \quad (3)$$

49 where δ is slip magnitude and λ_{min} is the minimum wavelength that is present in the fault
 50 profile (other symbols are defined in Table 1). The spatial extent of the slip patch must
 51 be much larger than λ_{min} for this to be valid. Roughness drag can be generalized to self-
 52 affine fault [12], but here I focus on the strictly self-similar case. In Section 3.1.1, I will
 53 use roughness drag to understand the certain rupture characteristic of the simulations in a
 54 quantitative manner.

55 Typically real faults are found to have α in the range of $10^{-3} - 10^{-2}$ [2]. The value
 56 likely depends on the maturity (cumulative amount of slip) of a fault, which the upper limit
 57 corresponding to less mature faults [4]. In this study, I have taken $\alpha = 0.01$, thus possibly
 58 representing an immature fault. This choice of α is also motivated by computational reasons
 59 since it allows interesting effects of the roughness to manifest at smaller length scales. Some
 60 studies found fault surfaces to be largely self-affine with a $H = 0.8$ in the direction of slip,
 61 but with a different slope at other scales [5]. However, it has been argued that a self-similar
 62 scaling ($H = 1$) can well fit all resolvable scales simultaneously [8].

63 The roughness drag τ_{drag} (Eq. 3) has α^2 dependence on amplitude-to-wavelength ratio,
 64 for small α the drag could be assumed small. However, the roughness drag also depends on
 65 δ/λ_{min} . Implying that τ_{drag} diverges as $\lambda_{min} \rightarrow 0$ for all non-zero values of α . Clearly if
 66 λ_{min} is sufficiently small, yielding of the material will occur as δ increases, thus limiting the
 67 roughness drag resistance. Fang and Dunham (2013) [7], suggested this may occur when
 68 $\delta/\lambda_{min} \approx 1$. The fact that faults are found to be rough over virtually all scales suggests that
 69 λ_{min} may be very small and may, therefore, be an important contributor to τ_{drag} , at least
 70 up to a point when yielding occurs, that is why I have chosen to focus on λ_{min} in this study.

Table 1: Reference parameters that are kept constant in the study

Symbol	Description	Value
<i>Material properties</i>		
ν	Poisson's ratio	0.25
μ	Shear modulus	30 GPa
c_s	Shear wave speed	3.5 km/s
<i>Friction</i>		
d_c	Characteristic state evolution distance	100 μm
a	Rate dependence of friction	0.01
b	State dependence of friction	0.0125
V_0	Steady state sliding velocity	10^{-9} m/s
f_0	Steady state coefficient of friction at V_0	0.6
σ'_0	Initial effective normal stress	100 MPa
<i>Fault</i>		
α	Amplitude-to-wavelength ratio	0.01
L	Fault length along x-axis	10 km
<i>Other parameters dependent on parameters above</i>		
L_∞	Critical crack half-length	$\frac{\mu d_c}{\pi(1-\nu)\sigma_0 b} \cdot \left(\frac{b}{b-a}\right)^2 \approx 29.3825$ m†
$b - a$	Degree of rate-weakening	0.0025
η	Radiation damping	$\mu/(2c_s) \approx 4.2857$ MPa · s/m † †
τ_0	Initial shear stress	$f_0\sigma_0 + \eta V_0 \approx 60.0000$ MPa
θ_0	Initial state	$d_c/V_0 \cdot (1 + \mathcal{N}(0, 0.01))$
<i>Notes</i>		
†	[18]	
††	[14]	
$\mathcal{N}(m, s)$	Gaussian noise, mean m , std. s	

71 2. Model Description

72 I use a boundary element method to mesh a fault surface $h(x)$ (Figure 1). The slip
 73 on each element (or dislocation) is assumed to be tangential to $h(x)$ (Figure 1d). That is,
 74 the dislocation is tilted at an angle $\theta = \arctan(dh/dx)$. By use of analytical solutions for
 75 elastic dislocations in full-space [19] I compute a matrix of influence coefficients that relate
 76 slip vector $\boldsymbol{\delta}$ and changes in shear $\boldsymbol{\tau}$ and normal stress $\boldsymbol{\sigma}$ at the center of each dislocation:

$$\boldsymbol{\tau}' = \mathbf{G}_\tau \boldsymbol{\delta}' \text{ and } \boldsymbol{\sigma}' = \mathbf{G}_\sigma \boldsymbol{\delta}', \quad (4)$$

77 where the meaning of $\boldsymbol{\delta}'$ versus $\boldsymbol{\delta}$ is discussed later. The matrices of influence coefficients are
 78 compressed using the H-matrix approach of Bradley and Segall (2011) [20]. The frictional
 79 interface is governed by rate-and-state friction and aging law, respectively:

$$\frac{\tau_0 + \boldsymbol{\tau}' - \eta \mathbf{V}}{\sigma_0 + \boldsymbol{\sigma}'} = f_0 + a \log\left(\frac{\mathbf{V}}{V_0}\right) + b \log\left(\frac{V_0 \boldsymbol{\theta}}{d_c}\right) \quad (5)$$

$$\dot{\boldsymbol{\theta}} = 1 - \frac{\boldsymbol{\theta} \cdot \mathbf{V}}{d_c}, \quad (6)$$

80 where \mathbf{V} and $\boldsymbol{\theta}$ represent the slip speed and state at the center of each dislocation respec-
 81 tively. Eq. 5 can be rearranged to provide an approximation for the slip speed at time step
 82 $n + 1$ given that the relevant fields are known at time step n .

$$\mathbf{V}_{n+1} = V_0 \exp\left(\frac{\boldsymbol{\tau}_n - \eta \mathbf{V}_n}{a \boldsymbol{\sigma}_n} - f_0/a - \frac{b}{a} \log(V_0 \boldsymbol{\theta}_n/d_c)\right), \quad (7)$$

83 where $\boldsymbol{\tau}_n = \tau_0 + \boldsymbol{\tau}'_n$ and $\boldsymbol{\sigma}_n = \sigma_0 + \boldsymbol{\sigma}'_n$. It is worth noting that at very high slip speeds (\sim
 84 1 cm/s) a few iteration are attempted where \mathbf{V}_n is slightly adjusted to better satisfy Eq. 7,
 85 otherwise spurious oscillations will appear. The state variable is integrated as

$$\boldsymbol{\theta}_{n+1} = \boldsymbol{\theta}_n + dt_n (1 - \boldsymbol{\theta}_n \mathbf{V}_n/d_c). \quad (8)$$

86 The time step determined by

$$dt_{n+1} = \min([\epsilon d_c / \max(\mathbf{V}_n), \epsilon \min(\boldsymbol{\theta}_n)]), \quad (9)$$

87 where ϵ is adjusted such that stability and convergence is found. The slip is updated as at
 88 each time step: $\delta_{n+1} = \delta_n + dt_n \mathbf{V}_n$. The problem is initialized such that $\boldsymbol{\tau} = \tau_0$, $\boldsymbol{\sigma} = \sigma_0$
 89 and $\boldsymbol{\theta} = d_c/V_0(1 + \mathcal{N}(0, 0.01))$ at all dislocation centers (See Table 1). The fault is thus
 90 approximately at steady state $\mathbf{V} = V_0$ initially apart from small amplitude Gaussian white
 91 noise added to the initial state. A planar infinite fault with the same frictional properties
 92 will oscillate around V_0 as long as the long term average of the elastic stress transfer is
 93 $\boldsymbol{\tau}' = 0$. This is reasonable, otherwise the long term average velocity of the fault would be
 94 changing, which can only occur if the loading is changed. The problem is more complicated
 95 for a non-planar and/or finite faults if the medium doesn't dissipate the stresses (which is
 96 the case for a perfectly elastic solid) then as $\boldsymbol{\delta}$ increases so do the stresses. However, the
 97 stresses in the medium and on the fault must on average relax at the same rate as the loading
 98 rate, otherwise they would simply build up indefinitely. I approximate this process using
 99 the backslip approach [21], where I have defined $\boldsymbol{\delta}' = \boldsymbol{\delta} - V_0 t$. Which is then used in Eq.
 100 4 to compute the elastic stress transfer. This approach differs from the RSQsim backslip
 101 implementation [21, 13], since I do not have to slip the faults backwards to determine the
 102 backslip stressing rate. I've simply formulated the problem such that the average steady
 103 state speed on the fault V_0 is also the loading rate.

104 The fault profile (Figure 1) is stochastically generated with a power spectral density
 105 in Eq. 2 using the implementation of Dunham et al., (2011) [6]. The dislocation length
 106 projected on the x-axis was set to 1 m. The smallest $\lambda_{min} \approx 10$ m and is thus resolved in the
 107 simulations. Frictional properties (see Table 1) are set such that the crack half-length which
 108 marks the transition from nucleation to a dynamic instability is constant $L_\infty \approx 30$ m and is
 109 therefore also well resolved. The fault profile was generated with λ_{min} ranging from $L_\infty/3$
 110 to $10 \cdot L_\infty$, but in all cases with the same random seed such that the Fourier decomposition
 111 at larger wavelengths is identical in both magnitude and phase.

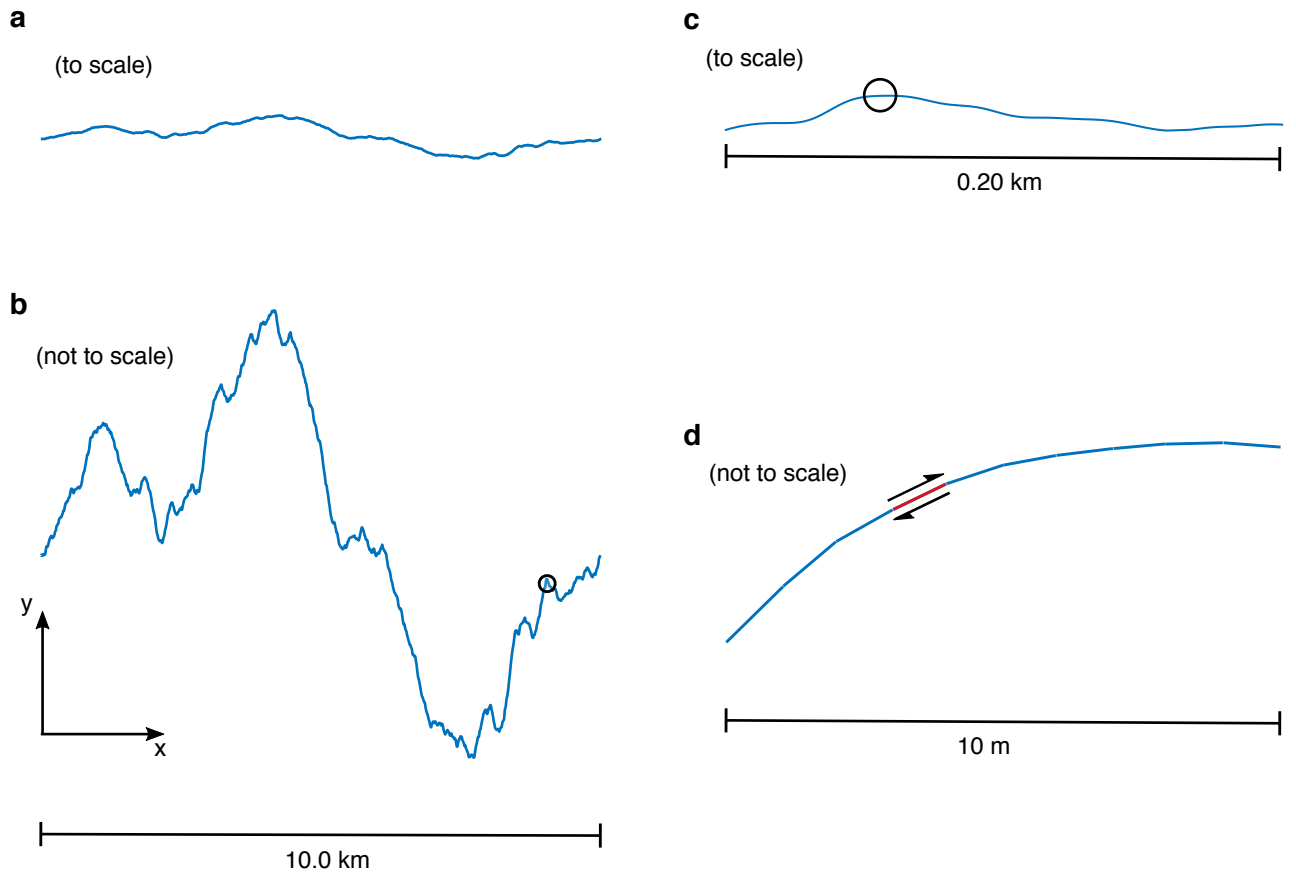


Figure 1: Fault profile at various scales for $\lambda_{min} = 2L_{\infty}/3$. **a** shows the entire fault at the correct length to amplitude ratio. **b** same as **a** except with exaggerated amplitude. Small circle shows the location of the fault segment shown in **c**. Circle in **c** shows the fault segment shown in **d** which displays the length scale of the discretization. Red segment shows the length of one dislocation sliding tangentially to the fault topography.

112 3. Results

113 3.1. Rupture characteristics

114 We start by visualizing the cumulative slip in all simulations (Figures 2, 3 and 4)

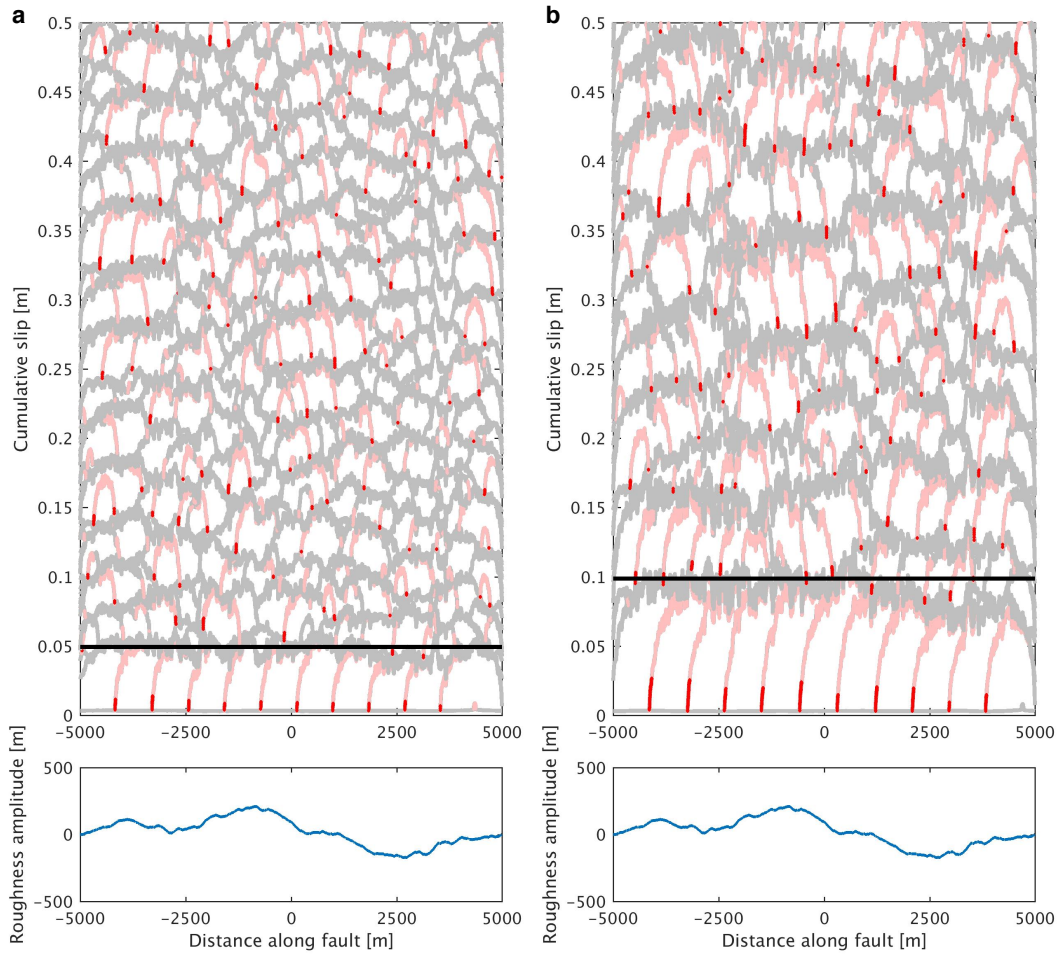


Figure 2: Snapshots of cumulative slip as a function of distance along fault. Red lines indicate points slipping faster than 1 m/s, pale pink lines indicate slip speeds larger than 1 cm/s. Grey lines are points slipping ≤ 1 cm/s. **a** shows results for $\lambda_{min} = L_{\infty}/3$, **b** shows results for $\lambda_{min} = 2L_{\infty}/3$. Bottom panels shows corresponding fault roughness, at the scale shown the fault profiles appear identical. Black line is the estimate of δ_c , the maximum slip distance estimate discussed in Section 3.1.1

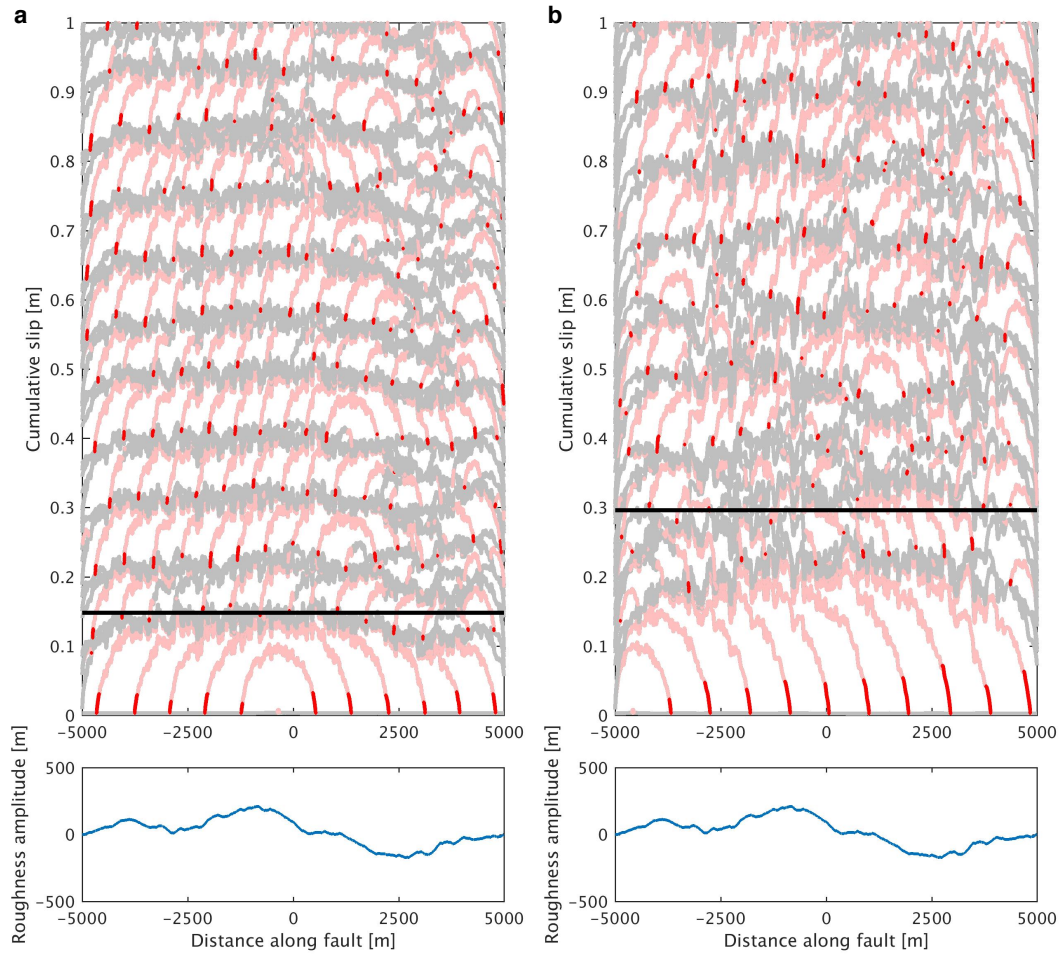


Figure 3: Same as Figure 2 except **a** shows results for $\lambda_{min} = L_{\infty}$, **b** shows results for $\lambda_{min} = 2L_{\infty}$. Note that the cumulative slip scale is different compared to Figure 2.

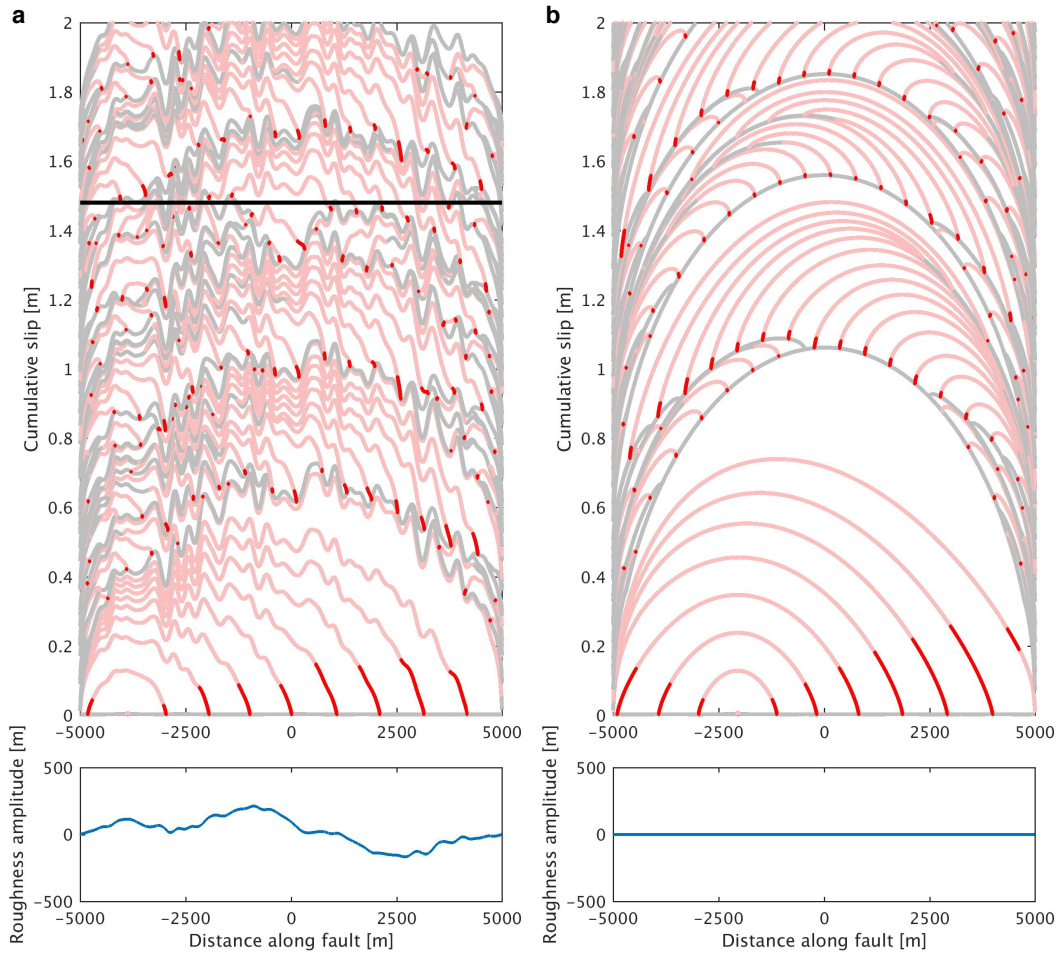


Figure 4: Same as Figure 2 except **a** shows results for $\lambda_{min} = 10L_{\infty}$, **b** shows a reference simulation of a planar fault. Note that the cumulative slip scale is different compared to Figures 2 and 3. No δ_c value exists for a planar and maximum slip distance is determined by fault finiteness and frictional properties, for **a** δ_c , significantly over-predicts the maximum slip distance because fault finiteness becomes the limiting factor before slip reaches δ_c .

115 From the slip profiles above we observe that initially the rupture always propagates
 116 the whole length of the fault. However, later events tend to be partial ruptures except
 117 when λ_{min} is large (Figure 4). Initially, the shear and normal stresses are selected to be
 118 spatially uniform, and the stress changes due to geometric complexity induced by the ac-
 119 tively propagating rupture are not sufficient to arrest the rupture. Once the initial rupture

120 has terminated, the resulting heterogeneous stress field can arrest ruptures and limits the
 121 event sizes. The results thus suggest that the assumed initial stress field in single rupture
 122 simulations on rough faults may be the primary control on the resulting rupture dimensions.

123 Another important observation from the simulations is that if events become sufficiently
 124 large, they transition from being crack-like to pulse-like, once they transition to pulse-
 125 like propagation, the events lock in an approximately fixed amount of slip. This is clear
 126 in simulations reported in Figures 2 and 3, whereas the fault in Figure 4a isn't sufficiently
 127 large to show this transition and is qualitatively similar to the planar fault simulation (Figure
 128 4b). The crack to pulse transition suggests that ruptures may have reached a length scale at
 129 which roughness drag becomes important (Eq. 3). In the next subsection, I further analyze
 130 the transition from a crack to pulse.

131 *3.1.1. Crack to pulse transition*

132 Let us hypothesize that transition from crack to pulse occurs approximately when the
 133 stress drop is equal to the roughness drag $\Delta\tau = \tau_{drag}$. Under these conditions it cannot be
 134 energetically favorable for a fault patch to slip further. Assuming a simple constant stress
 135 drop in-plane crack of half-length L_c then $\Delta\tau = (2\mu\bar{\delta})/(\pi(1-\nu)L_c)$, where $\bar{\delta}$ is the average
 136 slip. Setting $\Delta\tau = \tau_{drag}$ provides:

$$L_c = \frac{\lambda_{min}}{4\pi^4\alpha^2}, \quad (10)$$

137 which we interpret as a characteristic length scale for the crack to pulse transition. Re-
 138 markably, this scale only depends on roughness parameters λ_{min} and α^2 and not mechanical
 139 properties of the host rock and not the friction law, as long as the friction law favors in-
 140 stabilities that become crack-like. By comparing L_c to slip speed profiles during pulse-like
 141 propagation, we find that L_c well characterizes the dimension of the slip patch that is slipping
 142 approximately fast enough to radiating seismic energy (Figure 5). We may thus consider L_c
 143 as a characteristic dimension of the pulse. These results suggest that we may estimate L_c
 144 and therefore λ_{min}/α^2 from dynamic slip models that resolve pulse-like propagation ([e.g.
 145 22]). However, it is worth noting for a 3D rough surface L_c may be different, at least in

146 terms of prefactor. Further, other mechanisms can result in the manifestation of slip pulses
 147 on faults, such as low-stress conditions [23], or linear stability at large wavelengths due to
 148 slip to normal stress coupling [24], which may be responsible for generating the observed
 149 pulses in nature. It can be shown, although omitted here, that by including roughness drag
 150 in a linearized stability analysis using rate-and-state friction [e.g. 25], that large wavelengths
 151 become stable (although not related to normal stress changes). This also gives a length scale
 152 $\propto \lambda_{min}/\alpha^2$, albeit with a different prefactor than L_c .

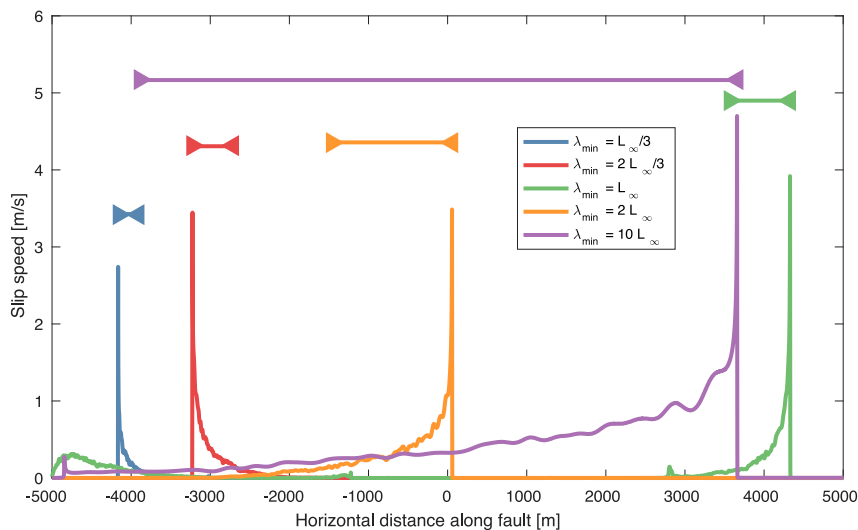


Figure 5: Comparison of L_c (horizontal lines, Eq. 10) to snapshots of slip speeds during pulse-like propagation during each simulation. The figure suggests that L_c is a good measure of a characteristic pulse length.

153 We may now use details of the rate-and-state friction law to estimate the maximum
 154 slip distance during pulse-like propagation. Once pulse reaches a point on the fault, we
 155 expect that friction rapidly evolves towards steady-state [18]. Locally the stress drop can
 156 be approximated as $\Delta\tau_{RS} \approx (b - a)\sigma_0 \log(V_d/V_0)$, where V_d could be considered a peak slip
 157 speed, here we shall take $V_d = 5$ m/s, thus $\log(V_d/V_0) \approx 22.3$. By virtue of the slow growth
 158 of the logarithm function, a minor error is introduced even if V_d is an order of magnitude
 159 smaller (in which case $\log(V_d/V_0) \approx 20.0$). Equating $\Delta\tau_{RS} = \tau_{drag}$ reveals a maximum slip

160 distance δ_c before we expect roughness drag to prevent further slip

$$\delta_c = \lambda_{min} \frac{1 - \nu (b - a) \sigma_0 \log(V_d/V_0)}{\mu 8\pi^3 \alpha^2}, \quad (11)$$

161 which suggests that in a single event, $\delta \lesssim \delta_c$. The corresponding values of δ_c are plotted as
162 black horizontal lines in Figures 2, 3 and 4 for each simulation and show excellent agreement
163 with the slip magnitude in the initial event in all cases where the fault was sufficiently large
164 to manifest the crack to pulse transition properly. The crack to pulse transition reported
165 here resembles the changes in the slip distribution of simple static crack calculations done
166 by Dieterich and Smith (2009) [26] as the crack size was increased. They also reported a
167 maximum slip distance with the same dependence on λ_{min}/α^2 as Eq. 11. However, their
168 formulation included an unknown fitting coefficient, whereas here no fitting is done.

169 *3.2. Seismicity and statistics*

170 As seen in Figures 2, 3 and 4 a single rough or planar fault can host a large distribution
171 of event sizes. In this section, I investigate the characteristics and statistics of the seismicity
172 in each simulation, in particular, the seismic moment distribution.

173 To extract discrete events from the simulations some assumptions need to be made about
174 the dimension and timing of each event. The following criteria are used for identifying a
175 single event and estimate seismic moment.

- 176 1. Identify a time period where the fault continuously slips at any point faster than 10
177 cm/s.
- 178 2. Find points where slip during that time was larger than d_c .
- 179 3. Compute the length of rupture and square to get area.
- 180 4. Compute the average change in slip where slip exceeded d_c .
- 181 5. Compute the seismic moment and magnitude

182 Clearly squaring the length of a rupture to obtain area is very simplistic and is only
183 valid if the aspect ratio of the ruptures are constant and other 3D effects, such as those that

184 might arise from event interactions, can be ignored. However, this provides a systematic
 185 way to compare our in-plane simulations to 3D observations.

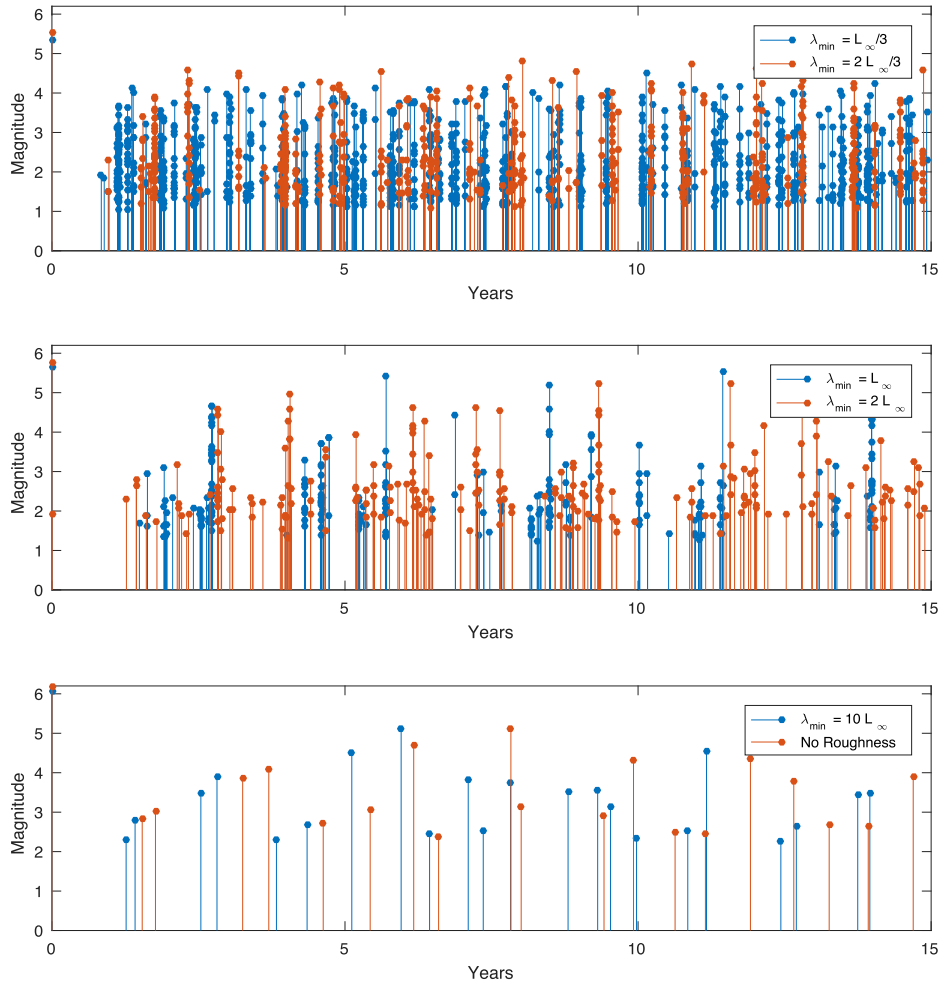


Figure 6: Magnitude versus time in all simulations for the first 15 years of simulations. For small λ_{min} , events are generally smaller and more numerous compared to larger λ_{min} values. Comparison of $\lambda_{min} = 10L_{\infty}$ and the no-roughness simulation reveals qualitatively similar behavior. The simulations indicated that there is both a maximum and minimum magnitude of events, which change with λ_{min} .

186 Figure 6 reveals very different frequency and magnitudes of seismicity for cases where
 187 λ_{min} is smaller or comparable to L_{∞} . If $\lambda_{min} \gg L_{\infty}$, the results suggest that the rough fault
 188 and planar fault are qualitatively similar in terms of the frequency, timing, and magnitudes
 189 of event. Further, Figure 6 suggests that each simulation has a minimum and maximum

190 moment event. The maximum moment is easy to understand since slip cannot exceed δ_c
 191 (Eq. 11), and the fault has a finite length. The minimum moment size is more mysterious
 192 since by decreasing λ_{min} the minimum moment also decreased. However, by decreasing λ_{min} ,
 193 the nucleation dimension should increase, which would imply that the smallest event size
 194 should increase [10]. A possible explanation comes from Eq. 11 where the slip distance is
 195 reduced, thus limiting the sizes of the events. That explanation is not fully satisfying since
 196 the smallest events in the simulations tend to arrest before reaching a slip distance of δ_c . A
 197 more likely explanation may be that due to residual stresses, if λ_{min} is decreased, the normal
 198 stress is locally increased at shorter wavelengths and thus locally the nucleation dimension
 199 is reduced. This finding highlights the importance of the initial stress in the analysis of
 200 earthquake nucleation on rough faults.

201 If the simulations presented, have any resemblance to earthquakes in nature, we expect
 202 that the moment distribution of events to be a power-law. Let us compare the empirical
 203 probability distribution function (PDF) to a theoretical moment distribution[27]:

$$\text{PDF}(M) = \frac{M_{max}^\beta M_{min}^\beta}{M_{max}^\beta - M_{min}^\beta} \beta M^{-1-\beta}, \text{ where } M_{min} \leq M \leq M_{max}, \quad (12)$$

204 where M is the moment and $\beta = 2b/3$, with b being the b value of the Gutenberg-Richter
 205 distribution, where typically $b \approx 1$. For comparison with simulation we have chosen a
 206 truncated moment distribution since we have inferred from Figure 6 that each simulation
 207 has both a minimum and maximum moment. Comparison of the theoretical PDF (Eq. 12)
 208 and the empirical PDF determined from each simulation shows that the two are in generally
 209 in good agreement for $b = 0.5$ (Figure 7), which well characterizes the fall-off with increased
 210 moment. It generally appears λ_{min} does not control the fall-off, but as has been previously
 211 noted, the truncation of the distribution is changed by λ_{min} . It is notable that even for the
 212 no-roughness limit, the events follow the same power-law distribution. This is consistent
 213 with recent work [28], which showed in simulations and theory that a planar fault that is
 214 sufficiently large could manifest a power-law distribution of events (see further discussion in
 215 Section 4.1). Some interesting differences are found in Figure 7, when comparing the cases

216 of $\lambda_{min} \lesssim L_\infty$ to $\lambda_{min} = 10L_\infty$ and the no-roughness case. We notice that at low values of
217 moments the empirical distribution has gaps for $\lambda_{min} = 10L_\infty$ and the no-roughness case,
218 whereas all gaps for $\lambda_{min} \lesssim L_\infty$ occur at high moment bins when events are rare. The
219 latter is most likely due to biased sampling. The synthetic catalog includes approximately
220 the maximum event size since it is the first event that occurs (Figure 2, 3 and 4), but due
221 to very numerous small events that increase computational time in these cases, it was not
222 feasible to simulate long enough sequences that would realize these rare events. However,
223 for $\lambda_{min} = 10L_\infty$ and the no-roughness case gaps occur at event sizes that should have been
224 realized in the catalog. For a larger L/L_∞ ratio these gaps might disappear. The gaps in the
225 PDF for a planar fault in Figure 7 are consistent with the bifurcation diagrams by Barbot
226 (2019)[29], which suggest that certain values of intermediate seismic moments do not occur.
227 Based on the results in this paper I hypothesize that rough faults may be ergodic in the
228 sense that if a single simulation is run for long enough events of all possible moments are
229 realized. However, a planar fault simulation will only realize a subset of the distribution
230 of possible moments and are thus not ergodic. I conclude that more study of this topic is
231 needed, in particular in 3D.

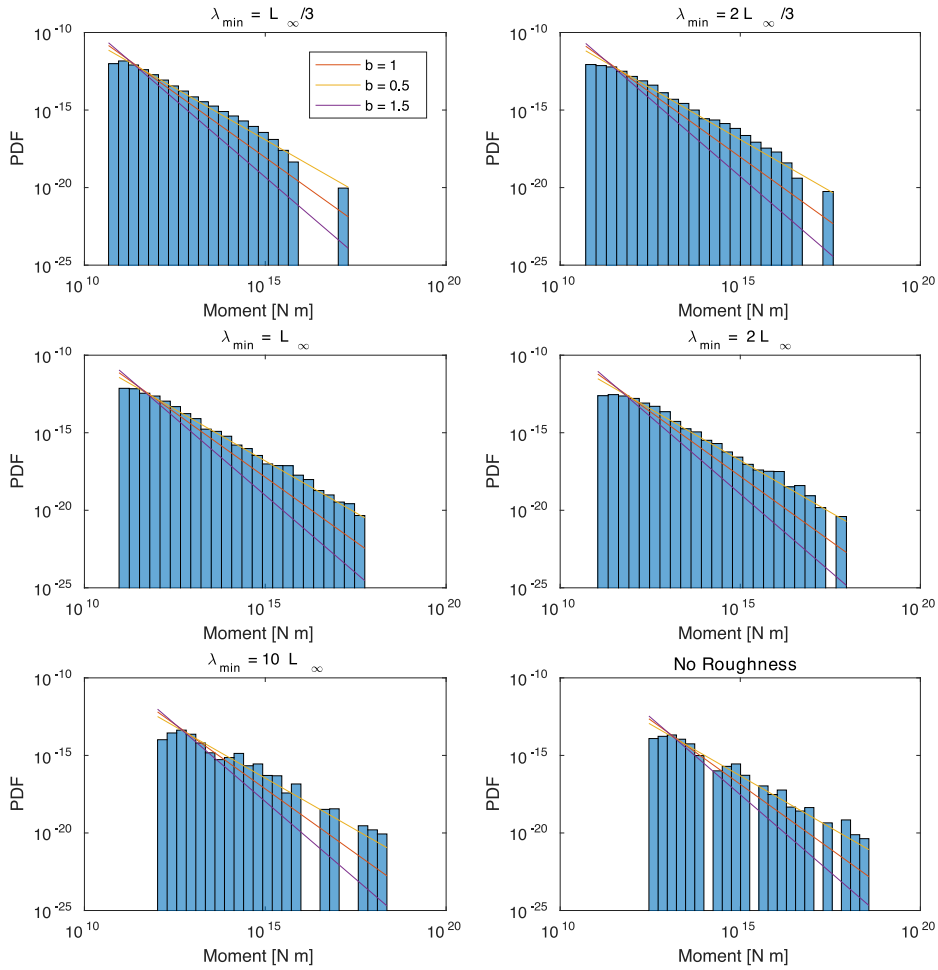


Figure 7: Comparison of Eq. 12 and the empirically estimated moment PDF function. The maximum and minimum moments in Eq. 12 are taken as the observed maximum and minimum moments in the simulations. Eq. 12 is plotted for $b = 0.5, 1, 1.5$, the comparison shows that a good agreement between empirical and theoretical PDFs is found for $b = 0.5$

232 4. Discussion

233 4.1. The b value

234 The b value most consistent with the simulations seems to be $b = 0.5$, which is consid-
 235 erably larger than the typically observed value of $b = 1$ value. The results suggest that the
 236 value is not related to the roughness since the same value is found for a planar fault, at
 237 least for $H = 1$. Cattania (2019) [28] analyzed an anti-plane fault loaded from below by a

238 creeping velocity strengthening section and bounded from above by a free surface. Through
239 theoretical considerations of simple crack models, she argued $b = 3/4$, which was supported
240 by simulations. This value is also somewhat larger than typically observed. Cattania (2019)
241 squared the rupture lengths to attain an area, as was done here. The simplistic treatment
242 of 3D effect is thus not the source of the difference, although it may factor into what value
243 of b is determined from the simulations. The main difference in this study compared to
244 Cattania (2019) is in the fault loading, here I have simulated a finite in-plane fault that is
245 loaded using backslip, whereas Cattania (2019) loaded by deep creep and stress build-up at
246 the top was prevented by a free surface. I suggest that the difference in loading is likely the
247 cause of the difference in b value, but I conclude that this issue needs further attention since
248 it may provide insight into the physical interpretation of b .

249 *4.2. The backslip approach*

250 The backslip approach to loading and dissipating stresses is a very efficient way of sim-
251 ulating earthquake cycles for geometrically complex faults. One can argue that stresses on
252 and off faults in the earth must dissipate on average over multiple cycles at the same rate
253 as the stresses build-up due to loading. Otherwise, stress accumulation would diverge. The
254 backslip approach achieves this balance. However, the transient temporal and spatial evo-
255 lution of the stresses may not be as expected from a more rigorous model that considers
256 off-fault plasticity using a continuum model of plasticity [e.g. 30, 6, 8]. However, such con-
257 tinuum plasticity models may not be able to accurately represent an important source of
258 dissipation that occurs off the main fault on discrete structures such as fault branches [31].
259 Further developments of earthquake cycle simulations are needed before we can efficiently
260 simulate multiple cycles on rough faults with realistic stress dissipation mechanisms; in the
261 meantime, backslip offers a simple way to investigate these problems.

262 **5. Conclusions**

263 Roughness has an important influence on both individual ruptures and frequency and
264 magnitude characteristic of events. Events start as crack-like ruptures, but due to roughness

265 drag, they transition to pulse-like ruptures at a characteristic length-scale determined by
266 fault roughness alone and not frictional properties or material constants (Eq. 10). Pulses
267 lock in approximately spatially fixed slip distance (Eq. 11), which depends on the assumed
268 friction law and material properties. Fault roughness thus offers a plausible mechanism for
269 earthquakes to transition from cracks to pulses as they grow. I find that decreasing λ_{min} ,
270 decreases both the maximum and minimum event sizes observed in the cycle simulations,
271 however, does not appear to alter the inferred b values which remains the same even for a ref-
272 erence simulation using a planar fault. Much more numerous small events thus characterize
273 simulations with small λ_{min} compared to large λ_{min} simulation or planar fault simulations.
274 The first event in the simulations always ruptures the entire fault, but following events are
275 generally smaller partial ruptures. This difference suggests that the residual stresses induced
276 by fault roughness are paramount in determining subsequent events sizes. Caution is needed
277 when selecting the initial stress distribution for single rupture models on rough faults since
278 it may significantly influence event sizes. Finally, I've hypothesized that sufficiently rough
279 faults are ergodic, but planar faults are not, in the sense that a rough fault simulation if run
280 for long enough will manifest all possible events sizes, but a planar fault will only manifest
281 a subset of event sizes.

282 6. Acknowledgements

283 I want to thank Eric M. Dunham for helpful discussions rough faults. I partially con-
284 ducted this research while being supported by NASA Headquarters under the NASA Earth
285 and Space Science Fellowship Program (Grant NNX16AO40H).

286 References

- 287 [1] S. R. Brown, C. H. Scholz, Broad bandwidth study of the topography of natural rock surfaces, *Journal*
288 *of Geophysical Research: Solid Earth* 90 (B14) (1985) 12575–12582. doi:10.1029/JB090iB14p12575.
- 289 [2] W. L. Power, T. E. Tullis, S. R. Brown, G. N. Boitnott, C. H. Scholz, Roughness of natural fault
290 surfaces, *Geophysical Research Letters* 14 (1) (1987) 29–32. doi:10.1029/GL014i001p00029.
- 291 [3] W. L. Power, T. E. Tullis, Euclidean and fractal models for the description of rock surface roughness,
292 *Journal of Geophysical Research: Solid Earth* 96 (B1) 415–424. doi:10.1029/90JB02107.

- 293 [4] A. Sagy, E. E. Brodsky, G. J. Axen, Evolution of fault-surface roughness with slip, *Geology* 35 (3)
294 (2007) 283–286. doi:10.1130/G23235A.1.
- 295 [5] T. Candela, F. Renard, Y. Klinger, K. Mair, J. Schmittbuhl, E. E. Brodsky, Roughness of fault surfaces
296 over nine decades of length scales, *Journal of Geophysical Research: Solid Earth* 117 (B8). doi:
297 10.1029/2011JB009041.
- 298 [6] E. M. Dunham, D. Belanger, L. Cong, J. E. Kozdon, Earthquake ruptures with strongly rate-weakening
299 friction and off-fault plasticity, part 2: Nonplanar faults, *Bulletin of the Seismological Society of Amer-*
300 *ica* 101 (5) (2011) 2308–2322. doi:10.1785/0120100076.
- 301 [7] Z. Fang, E. M. Dunham, Additional shear resistance from fault roughness and stress levels on geo-
302 metrically complex faults, *Journal of Geophysical Research: Solid Earth* 118 (7) (2013) 3642–3654.
303 doi:10.1002/jgrb.50262.
- 304 [8] Z. Shi, S. M. Day, Rupture dynamics and ground motion from 3-d rough-fault simulations, *Journal of*
305 *Geophysical Research: Solid Earth* 118 (3) (2013) 1122–1141. doi:10.1002/jgrb.50094.
- 306 [9] L. Bruhat, Z. Fang, E. M. Dunham, Rupture complexity and the supershear transition on rough faults,
307 *Journal of Geophysical Research: Solid Earth* 121 (1) (2016) 210–224. doi:10.1002/2015JB012512.
- 308 [10] Y. Tal, B. H. Hager, J. P. Ampuero, The effects of fault roughness on the earthquake nucleation process,
309 *Journal of Geophysical Research: Solid Earth* 123 (1) (2018) 437–456. doi:10.1002/2017JB014746.
- 310 [11] Y. Tal, B. H. Hager, Dynamic mortar finite element method for modeling of shear rupture on frictional
311 rough surfaces, *Computational Mechanics* 61 (6) (2018) 699–716.
- 312 [12] S. W. Ozawa, T. Hatano, N. Kame, Longer migration and spontaneous decay of aseismic slip pulse
313 caused by fault roughness, *Geophysical Research Letters* 46 (2) (2019) 636–643. doi:10.1029/
314 2018GL081465.
- 315 [13] A. Allam, K. Kroll, C. Milliner, K. Richards-Dinger, Effects of fault roughness on coseismic slip
316 and earthquake locations, *Journal of Geophysical Research: Solid Earth* 0 (ja). doi:10.1029/
317 2018JB016216.
- 318 [14] J. R. Rice, Spatio-temporal complexity of slip on a fault, *Journal of Geophysical Research: Solid Earth*
319 98 (B6) (1993) 9885–9907. doi:10.1029/93JB00191.
- 320 [15] J. H. Dieterich, Modeling of rock friction: 1. experimental results and constitutive equations, *Journal*
321 *of Geophysical Research: Solid Earth* 84 (B5) (1979) 2161–2168. doi:10.1029/JB084iB05p02161.
- 322 [16] A. Ruina, Slip instability and state variable friction laws, *Journal of Geophysical Research: Solid Earth*
323 88 (B12) (1983) 10359–10370. doi:10.1029/JB088iB12p10359.
- 324 [17] Y. Tal, B. H. Hager, The slip behavior and source parameters for spontaneous slip events on rough
325 faults subjected to slow tectonic loading, *Journal of Geophysical Research: Solid Earth* 123 (2) (2018)
326 1810–1823. doi:10.1002/2017JB014737.

- 327 [18] A. M. Rubin, J.-P. Ampuero, Earthquake nucleation on (aging) rate and state faults, *Journal of Geo-*
328 *physical Research: Solid Earth* 110 (B11). doi:10.1029/2005JB003686.
- 329 [19] M. Nikkhoo, T. R. Walter, P. R. Lundgren, P. Prats-Iraola, Compound dislocation models (cdms) for
330 volcano deformation analyses, *Geophysical Journal International* (2016) ggw427.
- 331 [20] A. Bradley, P. Segall, Efficient numerical modeling of 3d, half-space, slow-slip and quasi-dynamic
332 earthquake ruptures, in: *AGU Fall Meeting Abstracts*, 2011.
- 333 [21] K. Richards-Dinger, J. H. Dieterich, Rsqsim earthquake simulator, *Seismological Research Letters* 83 (6)
334 (2012) 983–990.
- 335 [22] J. Galetzka, D. Melgar, J. F. Genrich, J. Geng, S. Owen, E. O. Lindsey, X. Xu, Y. Bock, J.-P. Avouac,
336 L. B. Adhikari, B. N. Upreti, B. Pratt-Sitaula, T. N. Bhattarai, B. P. Sitaula, A. Moore, K. W. Hudnut,
337 W. Szeliga, J. Normandeau, M. Fend, M. Flouzat, L. Bollinger, P. Shrestha, B. Koirala, U. Gautam,
338 M. Bhattarai, R. Gupta, T. Kandel, C. Timsina, S. N. Sapkota, S. Rajaure, N. Maharjan, Slip pulse
339 and resonance of the kathmandu basin during the 2015 gorkha earthquake, nepal, *Science* 349 (6252)
340 (2015) 1091–1095. doi:10.1126/science.aac6383.
- 341 [23] G. Zheng, J. R. Rice, Conditions under which velocity-weakening friction allows a self-healing versus a
342 cracklike mode of rupture, *Bulletin of the Seismological Society of America* 88 (6) (1998) 1466–1483.
- 343 [24] E. R. Heimonsson, E. M. Dunham, M. Almquist, Poroelastic effects destabilize mildly rate-strengthening
344 friction to generate stable slow slip pulses, *Journal of the Mechanics and Physics of Solids* 130 (2019)
345 262 – 279. doi:https://doi.org/10.1016/j.jmps.2019.06.007.
- 346 [25] J. R. Rice, N. Lapusta, K. Ranjith, Rate and state dependent friction and the stability of sliding
347 between elastically deformable solids, *J. Mech. Phys. Solids* 49 (9) (2001) 1865–1898.
- 348 [26] J. H. Dieterich, D. E. Smith, Nonplanar faults: Mechanics of slip and off-fault damage, in: *Me-*
349 *chanics, structure and evolution of fault zones*, Springer, 2009, pp. 1799–1815. doi:10.1007/
350 s00024-009-0517-y.
- 351 [27] Y. Y. Kagan, Seismic moment distribution revisited: I. Statistical results, *Geophysical Journal Inter-*
352 *national* 148 (3) (2002) 520–541. doi:10.1046/j.1365-246x.2002.01594.x.
- 353 [28] C. Cattania, Complex earthquake sequences on simple faults, *Geophysical Research Letters* 0 (0).
354 doi:10.1029/2019GL083628.
- 355 [29] S. Barbot, Slow-slip, slow earthquakes, period-two cycles, full and partial ruptures, and deterministic
356 chaos in a single asperity fault, *Tectonophysics* 768 (2019) 228171. doi:https://doi.org/10.1016/
357 j.tecto.2019.228171.
- 358 [30] E. M. Dunham, D. Belanger, L. Cong, J. E. Kozdon, Earthquake Ruptures with Strongly Rate-
359 Weakening Friction and Off-Fault Plasticity, Part1: Planar Faults, *Bulletin of the Seismological Society*
360 *of America* 101 (5) (2011) 2296–2307. doi:10.1785/0120100075.

361 URL <https://doi.org/10.1785/0120100075>

362 [31] X. Ma, A. Elbanna, Dynamic rupture propagation on fault planes with explicit representation of short
363 branches, *Earth and Planetary Science Letters* 523 (2019) 115702. doi:[https://doi.org/10.1016/
364 j.epsl.2019.07.005](https://doi.org/10.1016/j.epsl.2019.07.005).